Applied Catalysis B: Environmental 273 (2020) 119060

Contents lists available at ScienceDirect

Applied Catalysis B: Environmental

journal homepage: www.elsevier.com/locate/apcatb

Electrochemical reconstruction of ZnO for selective reduction of CO_2 to CO

Wen Luo[a,b,*], Qin Zhang[a,b], Jie Zhang[a,b], Emanuele Moioli[a,b], Kun Zhao[a,b], Andreas Züttel[a,b]

[a] *Laboratory of Materials for Renewable Energy (LMER), Institute of Chemical Sciences and Engineering (ISIC), Basic Science Faculty (SB), École Polytechnique Fédérale de Lausanne (EPFL) Valais/Wallis, Energypolis, Rue de l'Industrie 17, CH-1951 Sion, Switzerland*

[b] *Empa Materials Science & Technology, CH-8600 Dübendorf, Switzerland*

ARTICLE INFO

Keywords:
CO_2 reduction
Electrocatalysis
Local pH
ZnO derived catalysts
Reconstruction

ABSTRACT

Electrocatalytic conversion of CO_2 to valuable chemicals is a highly promising route to close the carbon cycle. Herein, Zn catalysts derived from electrochemical reconstruction of ZnO materials are presented as efficient CO_2-to-CO catalysts. We found that ZnO precursors with different morphologies (nanowires, nanoflowers, and nanoparticles) underwent deep electro-reconstruction and formed porous structures composed of hexagonal Zn crystals, regardless of their initial properties. Using ex-situ and in operando techniques, we revealed that metallic Zn is the active phase for CO_2-to-CO. Because of the large surface area and stable crystal structure resulted from the reconstruction, ZnO-derived catalysts are highly selective and stable, showing > 90% selectivity to CO and more than 18 h stability. The great potential of ZnO-derived catalysts for industrial applications was demonstrated in a flow reactor, where 91.6% Faradaic efficiency for CO at a current density of 200 mA cm^{-2} can be achieved at –0.62 V vs. RHE.

1. Introduction

The electrochemical reduction of CO_2 (CO_2RR) has attracted much attention in recent years as a potential strategy to store the renewable electricity in the form of chemicals and fuels. One of the advantages of CO_2RR is the possibility of producing a variety of products, such as CO, formic acid, hydrocarbons, and oxygenates. Among these reactions, CO_2-to-CO- has been proposed, based on comparative technoeconomic analyses, to be the most economically feasible [1,2]. Moreover, as an important industrial feedstock, CO can be further converted into liquid fuels through Fischer-Tropsch synthesis, methanol synthesis, or electrochemical reduction [1,3,4]. The practical application of this process requires a catalyst that can reduce CO_2 to CO at a low overpotential ($\eta < 1$ V) with a high current density (> 200 mA cm^{-2}) and faradaic efficiency (FE, > 90%) [1]. Various catalysts have been investigated over the last few decades and Zn has been found to be the only earth-abundant monometallic catalyst that can produce CO with appreciable selectivity [5–10]. Bulk Zn catalysts, however, require large overpotentials but show low reaction rates, due to their limited number of active sites [7]. To enhance the catalytic activity and CO selectivity, research efforts have focused on designing of nanostructured Zn catalysts, including dendritic Zn [11], hexagonal Zn [10], porous Zn [9,12–15], and Zn nanosheets [16–18]. Despite the fact that 90% FE for CO (FE_{CO}) has been achieved on several nanostructured Zn electrodes, high overpotentials ($\eta \sim 1$ V) are often required and the current densities are mostly limited to 30 mA cm^{-2} (Table S1), which is far from meeting the requirements of commercialization.

Oxide-derived metals are perhaps the most well-known electrocatalysts for CO_2RR, due to their promising catalytic properties, as well as simple preparation methods [5,19–24]. Oxide-derived metals such as Cu [19,22,20–24], Ag [21,25], and Au [5] have been successfully demonstrated as highly active and selective catalysts for CO_2RR. Their catalytic performance depends largely on the preparation methods (e.g., thermal [19,22], plasma [23,26], and chemical [20] oxidation), the initial properties of the oxides (e.g., oxide layer thickness [22] and morphology [27]), and the final states of the reduced metals (e.g., oxidation state [23] and crystal structure [27,28]). However, much less studies have applied oxide-derived Zn (OD-Zn) for CO_2RR, and even so, the only reported FE_{CO} are greatly varied (from 20% over OD-Zn supported on carbon fiber [8] to 83% over vacancy-rich ZnO catalyst [29]), but none of which is significantly higher than that of a Zn foil electrode (79.4% FE_{CO} in 0.1 M $KHCO_3$) [7]. While the intrinsic CO selectivity of Zn can be attributed to its appropriate binding strength towards reaction intermediates (e.g. *COOH and *H), diverse sites such as oxygen vacancies [29], edge sites [30], or oxidized Zn species [31] of the nanostructured Zn have been proposed as "better" active centers compared to the polycrystalline Zn for CO_2RR. Unfortunately, lacking of systematic studies, it is hard to reveal the active sites and the origin of

---

[*] Corresponding author at: Laboratory of Materials for Renewable Energy (LMER), Institute of Chemical Sciences and Engineering (ISIC), Basic Science Faculty (SB), École Polytechnique Fédérale de Lausanne (EPFL) Valais/Wallis, Energypolis, Rue de l'Industrie 17, CH-1951 Sion, Switzerland.
E-mail address: wen.luo@epfl.ch (W. Luo).

https://doi.org/10.1016/j.apcatb.2020.119060
Received 19 February 2020; Received in revised form 20 April 2020; Accepted 22 April 2020
Available online 26 April 2020

the improved performance of OD-Zn catalysts. In the end, these findings raise two critical questions: Are OD-Zn catalysts potentially viable for practical CO_2RR applications? Is there a universal factor that determines the catalytic performance of OD-Zn catalysts for CO_2RR?

Aiming to answer these questions, we prepared three different OD-Zn catalysts by electrochemical reduction of ZnO precursors with very different morphologies (nanowires, nanoflowers, and nanoparticles). We evaluated their CO_2RR performance in both H-cell and flow cell and demonstrated that OD-Zn catalysts are of great potential for practical applications due to their high activity, CO selectivity, and stability. We found that, unlike other OD-metal catalysts [19–21], ZnO experienced deep reconstruction during electrochemical reduction and formed hexagonal Zn crystals regardless of their initial properties. Moreover, we disclosed that the oxidation method and the morphology of ZnO did not influence the intrinsic CO_2 reduction performance but affected the electrochemical surface area of the reduced Zn electrodes, which played a dominant role in determining the geometric activity and CO selectivity.

2. Experimental

2.1. Preparation of Zn electrodes

Zn foil (99.95%) was cleaned sequentially with 2 M HNO_3, acetone, and deionized water before being used as a substrate to prepare the three different ZnO materials. The ZnO-1 sample was prepared using a hydrothermal method modified from previous work [32]. Typically, 5 pieces of Zn foils (1 cm × 0.5 cm) were put into autoclave containing 50 mL of an aqueous solution of 2 M NaOH and 0.4 M $(NH_4)_2S_2O_8$. After being sealed, the autoclave was heated in an oven at 150 °C for 2 h to obtain the final materials. The ZnO-2 sample was prepared by spray-coating of ZnO nanoparticles onto the Zn foil. A typical ink for spray coating contained 1.0 g ZnO nanoparticle dispersion (20 wt%, Sigma Aldrich), 0.5 g Nafion (5 wt%, Sigma Aldrich), 5.0 g Milli-Q water, and 13.5 g isopropanol. The final loading of ZnO was controlled at ~2.5 mg cm^{-2}. The ZnO-3 sample was synthesized by an electro-deposition method modified from a previous work [33]: the deposition was performed in a solution containing 0.01 M $Zn(NO_3)_2$ and 0.1 M KCl at 60 °C for 2 h at a current density of −4 mA cm^{-2}. The ZnO-based GDE was prepared by drop-coating a Sigracet 39BC carbon paper with a ZnO dispersion to obtain a ZnO loading of 0.5 mg cm^{-2}. Higher loading was not used, because too thick catalyst layer may block the micro-porous layer of the gas diffusion electrode and decrease the hydrophobicity of the electrode [34]. The ZnO dispersion contained 1.0 mg mL^{-1} of ZnO nanoparticles and 0.25 mg mL^{-1} of fluorinated ethylene propylene (FEP, 55 wt%, Fuell Cell Store) in isopropanol. The GDEs were heated at 300 °C for 0.5 h to remove the surfactant. All these electrodes were pre-reduced at −1.6 V vs RHE in CO_2 saturated 0.1 M $KHCO_3$ for at least 20 min to fully reduce ZnO to metallic Zn.

To investigate the correlation of pH with CO selectivity (Fig. 5d), two additional Zn electrodes with different morphologies were prepared through electrodeposition. The (B) sample in Fig. 5d was prepared by electrodeposition of Zn using 0.05 M $ZnCl_2$ at −20 mA cm^{-2} for 3 min (Fig. S10a). The (D) sample in Fig. 5d was prepared by electrodeposition of Zn using 0.1 M $ZnSO_4$ and 1.5 M $(NH_4)_2SO_4$ at −500 mA cm^{-2} for 20 s (Fig. S10b). Another two electrodes, (C) and (E) in Fig. 5d, were prepared by electroreduction of ZnO-1 and ZnO-2 at −0.8 V vs RHE in CO_2 saturated 0.1 M $KHCO_3$, respectively (Fig. S3).

2.2. Characterization of Zn electrodes

A FEI Teneo system and a FEI Tecnai G2 Spirit Twin system were used for the collection of SEM and TEM images, respectively. A Bruker D8 Advance system was used for XRD measurements. XPS analyses were performed using a SPECS system equipped with a monochromatic Al Kα X-ray source (1486.6 eV) and a Phoibos 150 NAP analyzer [35]. Ar sputtering was performed in the preparation chamber connected to the analysis chamber of XPS. Operando Raman measurements were performed using a custom-made three-electrodes electrochemical cell and a Renishaw micro-Raman spectroscope (532 nm laser, ×50 long working distance objective).

2.3. Electrochemical measurements

For H-cell measurements [6,36], CO_2 saturated 0.1 M $KHCO_3$ (pH 6.8) was the electrolyte with the as-prepared Zn electrode, Pt wire, and Ag/AgCl (3.0 M KCl, Autolab) electrode as the working electrode, counter electrode, and reference electrode, respectively. The catholyte was purged with CO_2 at 20 mL min^{-1} prior to and during the experiments.

For the flow cell tests [37,38], the experiments were performed in a three-chamber flow cell with channels of dimension 1.0 × 0.5 × 0.15 cm^3. The CO_2 flow rate was 100 mL min^{-1}. 1.0 M KOH was used as the catholyte and anolyte and the flow rates of the electrolyte were controlled at 5 mL min^{-1} via a peristaltic pump. The cathodic and anodic chambers were separated via a Sustainion anion exchange membrane.

An Autolab PGSTAT302N potentiostat was used for all electrochemical measurements. All potential values, recorded against an Ag/AgCl (3.0 M KCl) reference electrode, were converted to RHE scale and reported after the ohmic loss correction. Gaseous products were quantified using an online gas chromatograph (GC, SRI instruments 8610C). Liquid products were collected and analyzed after the reaction using a high-performance liquid chromatography (HPLC, Thermo Scientific, Dionex UltiMate 3000 Standard System).

2.4. Reaction–diffusion modeling

The increased local pH during the H-cell measurements was calculated through a reaction–diffusion model developed by Gupta et al. [39]. During CO_2RR, although the increased OH^- can be consumed by the following reactions:

$$CO_{2(aq)} + OH^- \leftrightarrow HCO_3^- \tag{1}$$

$$HCO_3^- + OH^- \leftrightarrow CO_3^{2-} + H_2O \tag{2}$$

these reactions are reversible and are limited by diffusive processes.

In our model (Scheme S1), the diffusion region is assumed to be 50 µm and the modelling was performed between $x = 0$ µm (bulk) and $x = 50$ µm (electrode surface) using the following equations:

$$\frac{\partial[CO_2(aq)]}{\partial t} = D_{CO_2}\frac{\partial^2[CO_2(aq)]}{\partial x^2} - [CO_2(aq)][OH^-]k_{1f} + [HCO_3^-]k_{1r} \tag{3}$$

$$\frac{\partial[HCO_3^-]}{\partial t} = D_{HCO_3^-}\frac{\partial^2[HCO_3^-]}{\partial x^2} - [CO_2(aq)][OH^-]k_{1f} - [HCO_3^-]k_{1r} - [HCO_3^-][OH^-]k_{2f} + [CO_3^{2-}]k_{2r} \tag{4}$$

$$\frac{\partial[CO_3^{2-}]}{\partial t} = D_{CO_3^{2-}}\frac{\partial^2[CO_3^{2-}]}{\partial x^2} + [HCO_3^-][OH^-]k_{2f} - [CO_3^{2-}]k_{2r} \tag{5}$$

$$\frac{\partial[OH^-]}{\partial t} = D_{OH^-}\frac{\partial^2[OH^-]}{\partial x^2} - [CO_2(aq)][OH^-]k_{1f} + [HCO_3^-]k_{1r} - [HCO_3^-][OH^-]k_{2f} + [CO_3^{2-}]k_{2r} \tag{6}$$

where t is time, D is the diffusion coefficient for a given species, x is the position within the boundary layer, and k_f and k_r are the reaction rate constants for forward and reverse reactions of (1) and (2), respectively. The rate constants were adopted from Gupta et al. [39] with $k_{1f} = 5.93 \times 10^3$ M^{-1} s^{-1}, $k_{1r} = 1.34 \times 10^{-4}$ s^{-1}, $k_{2f} = 1 \times 10^{-8}$ M^{-1} s^{-1}, and $k_{2r} = 2.15 \times 10^{-4}$ s^{-1}.

As H_2 and CO were detected with approaching 100% FE for our Zn catalysts, the concentration of OH^- at the surface of the electrode can

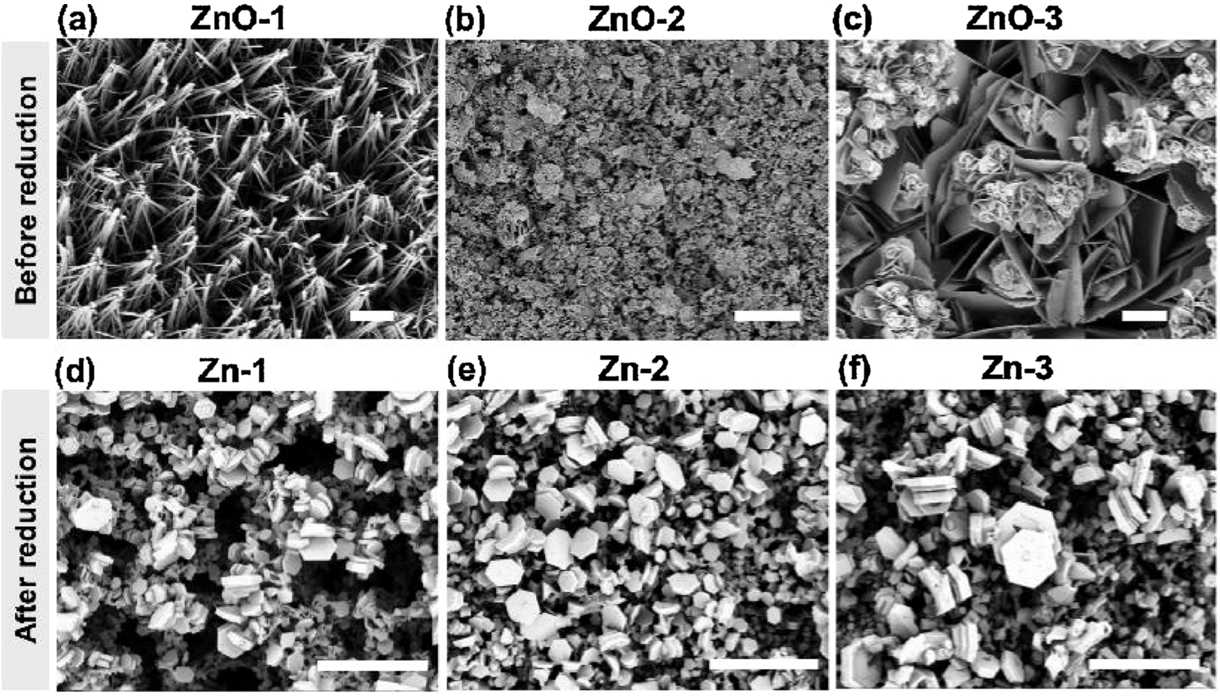

Fig. 1. SEM images of the ZnO samples prepared by (a) hydrothermal oxidation, (b) ZnO nanoparticle deposition, and (c) electrodeposition, and the corresponding reduced samples (d, e, and f). Scale bars in (a)–(f) are 2 μm.

be calculated as:

$$OH^{-}_{formation} = \frac{j}{F} \tag{7}$$

where *j* is the geometric current density and *F* is the faradaic constant. Using the boundary conditions and initial conditions suggested by Gupta et al. [39], the partial differential Eqs. (3)–(6) can be solved and the local pH values can be obtained.

3. Results and discussion

3.1. Characterization and reconstruction mechanisms of OD-Zn electrodes

Three ZnO materials were synthesized on Zn foil substrates using three different methods. Scanning electron microscope (SEM) images show that the ZnO-1 sample (Fig. 1a), resulting from hydrothermal oxidation of Zn foil, is homogeneously covered with nanowire arrays of ~5 μm in length and 100 − 200 nm in diameter. The ZnO-2 sample was prepared by spray-coating with ZnO nanoparticles. Due to the presence of Nafion as a binder, the nanoparticles are partially agglomerated (Fig. 1b). The electrochemically deposited sample (ZnO-3) shows a nanoflower morphology which is composed of thin flakes (~30 nm thickness) with sizes (widths) of ~1 − 5 μm (Fig. 1c).

The as-synthesized ZnO samples were electrochemically reduced at −1.6 V versus reversible hydrogen electrode (RHE) in CO_2 saturated 0.1 M $KHCO_3$ electrolyte, and the reduced samples were denoted as Zn-1, Zn-2, and Zn-3, respectively, corresponding to the ZnO-1, ZnO-2, and ZnO-3 precursors. Surprisingly, the morphologies of the OD-Zn samples are distinct from those of their ZnO precursors: all three OD-Zn samples show a porous morphology composed of thin hexagonal flakes (Fig. 1d–f). Transmission electron microscope and selected area diffraction results indicate that the hexagonal flakes are Zn single crystals with exposed (002) facets (Figure S1) [40]. Recently, reconstruction (e.g., fragmentation) of Cu oxides during CO_2RR has been observed but the process is crucially related to the initial state of Cu oxides [28,41], as in most cases, metal oxides can well preserve their initial morphologies even after long-term electrolysis [20,41–43]. Therefore, in contrast to other metal oxides, the morphology-independent reconstruction of ZnO may help to underline the universal factor that determines the catalytic performance of OD-ZnO.

To understand the morphology evolution process, SEM images of the three ZnO samples were taken after 2, 5, 10 and 15 min of electrochemical reduction, respectively (Fig. 2a and Fig. S2). As illustrated in Fig. 2b, small crystals (< 100 nm) start to form on the surface of the ZnO nanostructures after a few minutes of reduction. With the increase of reduction time, the size of the hexagonal crystals increase, and the morphology of the three ZnO samples all change to the porous morphology of hexagonal crystal assembly. We suggest that this structural reconstruction is due to the dissolution-reduction-crystallization process of ZnO, which starts from the dissolution of ZnO by forming soluble $Zn(OH)_4^{2-}$ ions [44,45], followed by the reduction of $Zn(OH)_4^{2-}$ to Zn and the growth of Zn crystals. The crystal shape of the Zn deposits mainly depends on the dissolution and re-deposition rate [46]. In CO_2 reduction environment, well-faceted hexagonal crystals are obtained because of the relatively slow overall reduction rate, which allows the formation of a shape that can reach a minimum surface energy. The reduction of ZnO at more positive potentials (e.g., −0.8 V vs RHE), therefore, leads to larger hexagonal crystals due to the slower crystallization rate, which, however, also results in lower porosities (Figs. S3 and S4). Moreover, the initial morphology of the ZnO precursor, which determines the distribution of nucleus centers and the local concentration of Zn^{2+} species, is found to affect the electrochemically active surface area (ECSA) of the obtained OD-Zn electrodes. According to the double layer capacitance measurements (Fig. S5), ZnO-1, with individually and vertically aligned nanowires, derives a catalyst (Zn-1) that has 1.5 and 2.3 times larger ECSA, respectively, than those of Zn-2 and Zn-3 do. Note that an even lower reduction potential (e.g., < −1.6 V vs RHE) is not applicable to all ZnO samples, as faster reduction rates and concomitantly generated H_2 bubbles may result in the exfoliation of the reduced Zn layer. Thus, −1.6 V vs RHE was chosen for the electro-reconstruction of ZnO for the following study.

The crystal structures of the as-prepared and reduced ZnO samples were studied using X-ray diffraction (XRD). As shown in Fig. 3a, diffraction peaks from ZnO and Zn can be observed for all three ZnO

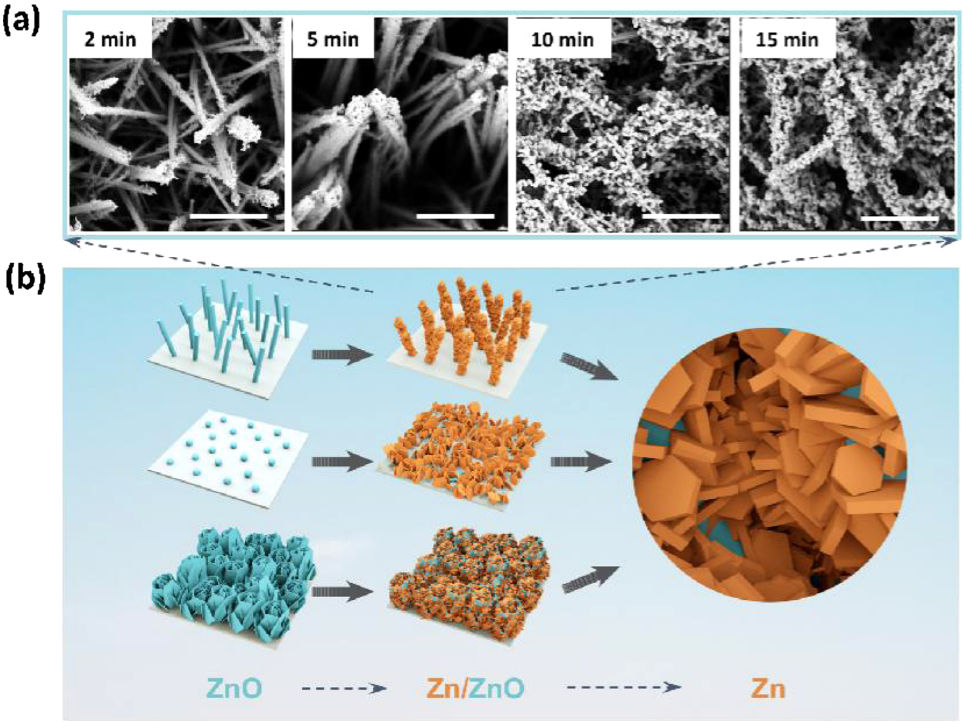

Fig. 2. (a) Typical SEM images of ZnO-1 sample reduced for 2, 5, 10 and 15 min at −1.6 V vs RHE in CO_2 saturated 0.1 M $KHCO_3$ electrolyte. (b) Schematic illustration of the electrochemical reconstruction process for three ZnO samples. Scale bars in (a) are 1 μm.

samples. The presence of well-defined ZnO peaks indicates the highly crystalline nature of the as-prepared ZnO samples. The peaks of metallic Zn are ascribed to the Zn foil used as the substrate. For the Zn-3 sample, low intensity peaks from $Zn_5(OH)_8Cl_2{\cdot}H_2O$ also appear due to incomplete dehydration during the electrodeposition process. After reduction, oxidized Zn species are reduced to metallic Zn as indicated by the absence of diffraction peaks from oxides. X-ray photoelectron spectroscopy (XPS) was performed to characterize the surface properties of the samples. Since it is difficult to distinguish Zn from ZnO in the Zn 2p region of the XPS spectrum due to their similar binding energies

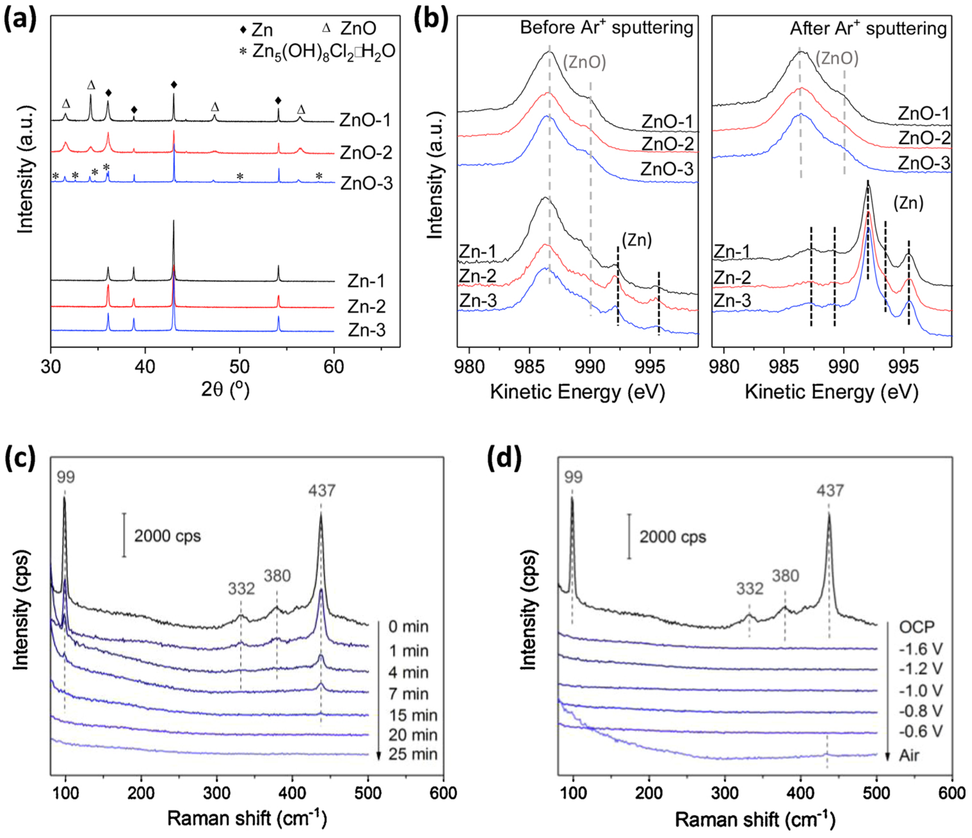

Fig. 3. (a) XRD patterns and (b) Zn LMM spectra of as-prepared and electrochemically reduced ZnO samples. Gray and black dash lines in (b) represent ZnO and Zn Auger peaks, respectively. Operando Raman spectra of (c) the ZnO-1 sample at different durations during the pre-reduction at −1.6 V vs RHE and (d) the ZnO-1 sample under various treatment conditions. The OCP in (d) represents open circuit potential, which is the same spectrum collected at 0 min in (c). The −1.6 V in (d) is the same spectrum collected at 25 min in (c). All Raman spectra were collected in CO_2-saturated 0.1 M $KHCO_3$, except the condition “Air” in (d).

[9], we compared the Zn LMM auger peaks of the as-prepared and reduced samples. As shown in Fig. 3b, all three ZnO samples exhibit the typical auger peaks of ZnO, with a main peak at ∼987 eV and a shoulder at ∼990 eV. After reduction, unexpectedly, only low intensity Zn peaks are present at ∼992 and ∼996 eV, while high intensity ZnO peaks still exist. This may result from the re-oxidation of Zn by air during the transfer of the OD-Zn into the XPS chamber, although the transfer process takes only a few minutes. To verify this hypothesis, we sputtered the catalysts with Ar^+ to remove the top layers of the catalysts. After sputtering, the ZnO samples still show typical auger spectra of ZnO, indicating that the Ar^+ sputtering process did not result in detectable reduction of ZnO. However, the ZnO peaks from OD-Zn samples are absent, confirming the removal of the air-oxidized thin oxide layer on OD-Zn.

Operando Raman spectroscopy was then performed to gain real-time insights into the reduction process of ZnO and the oxidation states of Zn during the CO_2 electroreduction. Fig. 3c shows the Raman spectra of a representative ZnO-1 sample held at pre-reduction condition (−1.6 V vs RHE) in CO_2 saturated 0.1 M $KHCO_3$. Before reduction (0 min), the characteristic Raman peaks of ZnO at 99 (E_{2L}), 332 ($E_{2H} - E_{2L}$), 380 (A_{1T}), and 437 (E_{2H}) cm^{-1} can be clearly observed [47,48]. During the first 15-min reduction, the intensity of ZnO peaks gradually decreased, indicating the partial reduction of top layers of ZnO to metallic Zn. This result agrees well with our SEM observations that because of the deep reconstruction, the surface of ZnO cannot be fully covered by the reduced Zn crystals within 15 min (Fig. 2a). After 20-min reduction, no peak from ZnO can be observed in the Raman spectra, demonstrating that the surface ZnO is completely reduced to metallic Zn. During the reduction process, we cannot observe signals of the reduction intermediates from ZnO or CO_2, possibly due to the short life time and/or the low coverage of these intermediates [49]. Fig. 3d shows the potential-dependent Raman spectra acquired at the steady state of each applied potential. The feature-less spectra at potentials between −0.6 and −1.2 V vs RHE indicate that Zn can maintain metallic state under the CO_2 electrolysis potentials. After exposing the reduced sample in air for several minutes, a weak ZnO peak appears at 437 cm^{-1} (Fig. 3d), suggesting the reduced Zn surface is easy to be oxidized by air, which further supports our XPS results.

Taken together, these results indicate that under CO_2RR conditions, ZnO sample tend to restructure into hexagonal metallic Zn crystals independent of their initial morphology. This reconstruction behavior implies that careful investigation of the final states of the nanostructured catalysts is essential in order to establish correct structure-performance relationships. The similar hexagonal crystal structure of the reduced Zn electrodes offers a platform to identify the key factors that influence the catalytic performance, while its energetically stable nature is important for a stable CO_2 reduction performance. Moreover, in light of the dramatically increased surface roughness in comparison to a flat Zn electrode, the OD-Zn electrodes are expected to show high CO_2RR activity.

3.2. CO_2 RR performances

The CO_2RR performances of the three OD-Zn catalysts were first evaluated in a customized H-cell with CO_2-saturated 0.1 M $KHCO_3$ as the electrolyte. As shown in Fig. 4a, the overall geometric current density (j_{geo}) of the three Zn catalysts increased with a decrease in the applied potential. At −1.0 V vs RHE, j_{geo} reached 18.5, 15.6, and 11.0 mA cm^{-2} for Zn-1, Zn-2, and Zn-3, respectively. These current densities are greatly improved compared to those of the bulk Zn catalysts, which are typically less than 3 mA cm^{-2} at −1.0 V vs RHE [9,30].

Gaseous and liquid products were analyzed using gas chromatography and high-performance liquid chromatography, respectively. Similar to other Zn-based catalysts, only CO and H_2 were detected as the primary products with total FEs of around 95% (Fig. 4b and c) [8,9,11]. Fig. 4b shows that all three catalysts are highly selective towards CO with exceeding 90% FE at moderate overpotentials (∼750 mV), which surpasses that of other nanostructured Zn catalysts (Fig. S6). The three OD-Zn catalysts also showed differences in selectivity: at a low overpotential range (−0.6 V to −0.8 V vs RHE), where the mass transport limitation is insignificant, the CO selectivity decreases in the order of Zn-1 > Zn-2 > Zn-3, similar to the trend of current density.

The long-term CO_2RR performance of the OD-Zn catalysts was evaluated at a constant current density of 3.0 mA cm^{-2}. As shown in Fig. 4d, all three catalysts exhibited remarkably stable potentials, and CO FEs were maintained at ∼85% for more than 18 h. The SEM images of the samples after the stability tests (Fig. S7) showed that the hexagonal crystals are well preserved, implying the high stability of those crystals under CO_2RR conditions. Overall, as expected from the above discussions, OD-Zn catalysts are of sufficient potential as promising catalysts for CO_2RR with superior activity, CO selectivity, and long-term stability.

3.3. Origin of the enhanced performance of OD-Zn electrodes

To shed light on the activity origin of OD-Zn, geometric partial current densities of CO ($j_{CO/geo}$) for the three OD-Zn samples and a Zn foil reference sample [9] were plotted in Fig. 5a. Due to the high j_{geo} and FE_{CO}, the $j_{CO/geo}$ values of Zn-1, Zn-2, and Zn-3 are on average 30, 19, and 14 times higher than that of the Zn foil, respectively. To deconvolute the influence of surface area, we normalized $j_{CO/geo}$ with the ECSA of the electrode. As shown in Fig. 5b, all four catalysts exhibited very similar ECSA-normalized CO partial current densities ($j_{CO/ECSA}$), indicating that the intrinsic activity of an OD-Zn catalyst is independent of the oxidation method, the initial morphology, and the crystal structure of ZnO. Moreover, it also implies that the bulk Zn electrodes may share similar types and densities of active centers as those of the OD-Zn. Considering that the size of the hexagonal flakes of OD-Zn ranges from 0.1 to 1 μm, these results are consistent with recent findings that the CO_2RR activity of Zn nanoparticles with size larger than 6 nm is comparable to that of the bulk Zn [50]. Therefore, we suggest that similar to Zn polycrystals, the catalytic center of OD-Zn is also metallic Zn, and the significantly improved geometric activities of OD-Zn are mainly attributed to the reconstruction induced high surface area.

Apart from the improved activity, OD-Zn catalysts also showed enhanced CO selectivity compared to the bulk Zn electrodes. Previous reports have proposed that surface oxidation [31], the presence of defects (e.g., oxygen-vacancies [29], grain boundaries [8], and under-coordinated sites [16,30]), preferential faceting (e.g. Zn(002)) [10,15,17,18], and the increase of local pH [9] are preferred for high CO selectivity. Interestingly, among these proposed mechanisms, both energetically stable sites (e.g., Zn(002) facet) and unstable sites (e.g., oxygen-vacancies and undercoordinated sites) have been identified as active centers, despite that most of these studies were performed in the same potential range (i.e., −0.6 to −1.2 V vs RHE) and in similar electrolytes (e.g., CO_2 saturated $KHCO_3$). These conflicting findings imply that a recessive factor undetectable by using conventional characterization techniques may play a more general role to enhance the CO selectivity for nanostructured-Zn catalysts.

Herein, we find that ZnO materials prepared using different methods can be readily reduced to metallic Zn crystals before CO_2RR (Fig. 3a−c), which can maintain the metallic state during CO_2RR (Fig. 3d). Thus, oxidized Zn species and oxygen-vacancies are not considered as active centers of our OD-ZnO samples for CO_2-to-CO. In addition, since all three OD-Zn samples are composed of highly crystallized Zn crystals, the number of defects and edge sites may be too low to dominate the FE_{CO} enhancement compared to, for example, the lithium-tuned Zn catalyst [8]. Notably, an increase in the content of low-coordinated sites on small Zn nanoparticles was found in a recent study to increase the H_2 production rate rather than the CO selectivity [50].

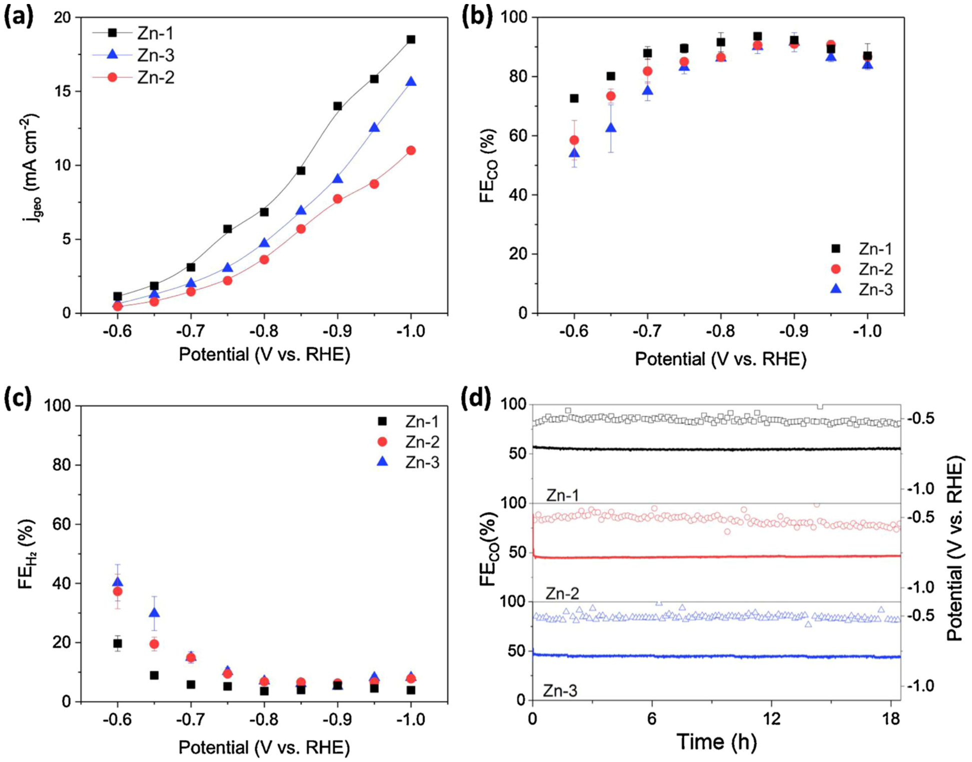

Fig. 4. (a) Current density, (b) CO FE and (c) H_2 FE of Zn-1, Zn-2 and Zn-3 in 0.1 M $KHCO_3$. (d) Long-term performance of Zn-1, Zn-2, and Zn-3 for CO_2RR at 3.0 mA cm^{-2}. Open symbols and lines in (d) represent FE_{CO} and applied potential, respectively. Error bars in (b) and (c) represent the standard deviation from three measurements.

Moreover, the exposing of the Zn(002) facet can be hardly correlated with the high FE_{CO}, as the control samples composed of larger and thinner hexagonal crystals did not show better CO selectivity (Fig. S8). Ruling out these factors, the pH at the electrode surface, which can be hardly measured directly but is linked to the surface area of the electrode, is more likely to be a critical factor. During CO_2RR, the local pH can increase due to the consumption of protons from both the H_2 evolution reaction (HER) and CO_2RR. Therefore, under an identical reaction environment (i.e., 0.1 M $KHCO_3$ electrolyte), this local pH change is proportional to the current density and thus to the electrode surface area. High local pH is suggested to improve the CO_2RR selectivity through suppressing HER, due to the fact that the HER rate is highly sensitive to the protonation environment [51–53]. Here, we also found that the ECSA-normalized HER activities of the OD-Zn catalysts were much lower than those of the Zn foil sample (Fig. S9), indicating that suppressed HER activity led to the high CO selectivity of OD-Zn.

To further verify the pH effects, we conducted a simplified reaction-diffusion model to estimate the pH near the surface of the electrode [39]. Fig. 5c compares the FE_{CO} and the local pH at −0.65, −0.7, and −0.75 V vs RHE for Zn foil, Zn-1, Zn-2, and Zn-3. The first observation

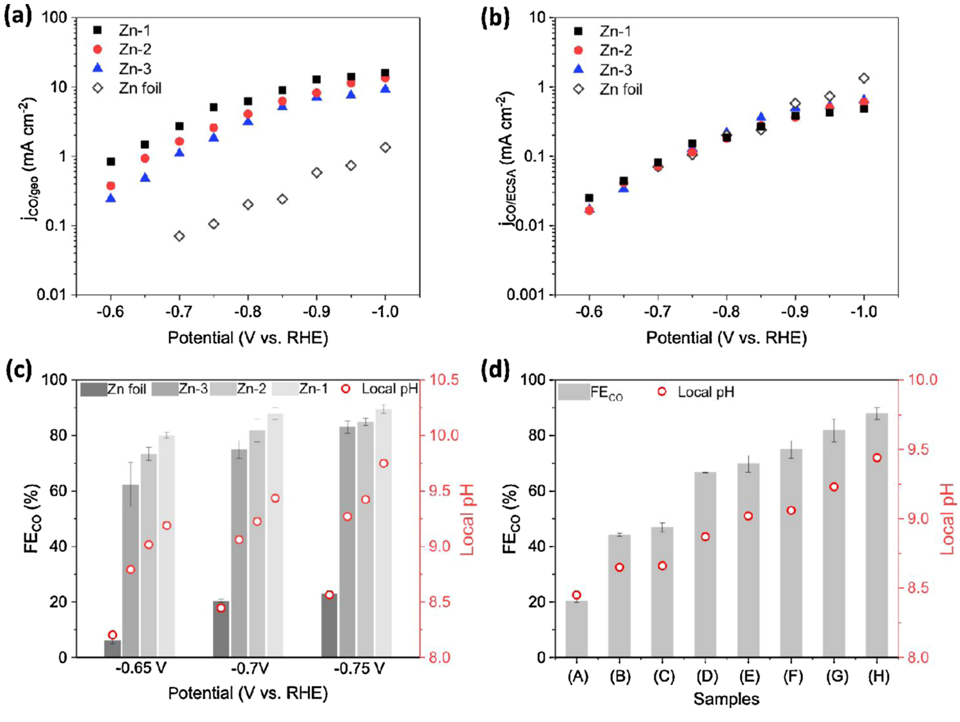

Fig. 5. CO partial current densities normalized by (a) geometric surface area and (b) electrochemical surface area for Zn-1, Zn-2, Zn-3, and Zn foil [9]. (c) FE_{CO} and local pH for each Zn electrode at different applied potentials. (d) FE_{CO} and local pH at −0.7 V for: (A) Zn foil, (B) Zn with irregular morphology, (C) ZnO-2 reduced at −0.8 V, (D) Zn dendrites, (E) ZnO-1 reduced at −0.8 V, (F) Zn-3, (G) Zn-2, and (H) Zn-1. Error bars in (c) and (d) represent the standard deviation from three measurements.

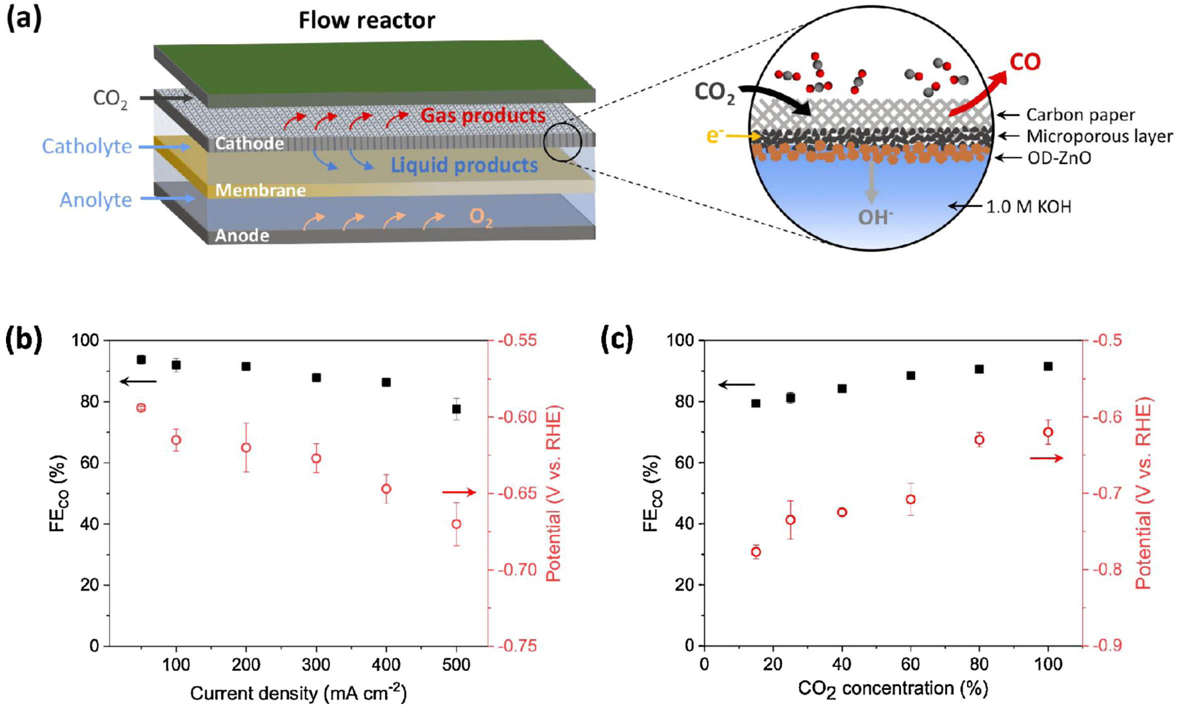

Fig. 6. (a) Illustration of the flow reactor and the OD-ZnO based GDE for CO_2RR. Faradaic efficiency for CO and cathode potential as a function of (b) current density (at 100% CO_2) and (c) different CO_2 concentrations (15–100% (vol/vol) using N_2 for dilution) (at a constant current density 200 mA cm^{-2}) using 1.0 M KOH. Error bars represent the standard deviation from three measurements.

from Fig. 5c is that all local pH values (> 8) are significantly higher than the bulk pH (6.8 for CO_2 saturated 0.1 M $KHCO_3$) even at this low overpotential range. Furthermore, at a given potential, the increasing trend of local pH corresponds well with the increase of ECSA (Zn foil < Zn-3 < Zn-2 < Zn-1), due to the fact that the OH^- formation rate (Eq. 7, Experimental section) is determined by the overall current density. More importantly, the good correspondence between FE_{CO} and local pH successfully demonstrates that the high local pH induced by the high surface area of OD-Zn enhanced the CO selectivity. In addition, we prepared several nanostructured Zn electrodes (Figure S3 and S10) and performed CO_2RR under identical conditions. As shown in Fig. 5d, the FE_{CO} monotonically increases with the local pH regardless of the sample morphology or preparation method. Despite that the aforementioned factors that related to the crystal structure or the oxidation state of Zn have be shown to affect the CO_2RR performance [8,16–18,29], our results indicate that the final ECSA of the OD-Zn electrode has a universal and significant effect on the catalytic performance. Thus, in combined with the ex-situ and in operando characterization results, we can conclude that metallic Zn is the catalytic center for CO_2RR, and the reconstruction induced higher surface area universally enhances the catalytic activity and selectivity. The difference in the initial morphology of ZnO, on the other hand, only affects the final ECSA of OD-Zn, hence leading to a different extent of performance improvement. Overall, as the electrochemical reconstruction of ZnO is a simple yet effective method to generate high surface area Zn catalysts for CO_2RR, future work can focus on the design of ZnO materials with proper morphologies and on the optimization of the reduction conditions to maximize the surface area of the final Zn electrodes.

3.4. Boosting the electrocatalytic performance in flow reactor

The potential of using OD-Zn for large scale applications was investigated using a microfluidic reactor (Fig. 6a), which circumvents the CO_2 mass transport limitation in H-cell reactors. As CO_2 and the electrolyte were separated in the flow reactor, 1.0 M KOH was used as an electrolyte to further increase the local pH to suppress HER. The gas diffusion electrode (GDE) was prepared by drop-coating of commercially available ZnO nanoparticles onto a carbon paper. The GDE was then pre-reduced at −1.6 V vs RHE in CO_2 saturated 0.1 M $KHCO_3$ electrolyte to reconstruct ZnO. As expected, hexagonal Zn crystals were observed (Figure S11), albeit with small size due to the low loading (0.5 mg cm^{-2}) and the high dispersion of ZnO on the carbon paper. As shown in Fig. 6b (Fig. S12 for product distribution), OD-Zn based GDE exhibited a superior CO_2 reduction performance: over 90% FE_{CO} was achieved at current densities up to 200 mA cm^{-2} and potentials more positive than −0.62 V vs RHE. In addition, we obtained a total current density of 500 mA cm^{-2} and a CO partial current density of 388 mA cm^{-2} (776 A $g_{ZnO}{}^{-1}$) at −0.67 V vs RHE. This performance rivals state-of-the-art noble-metal, single-atom, and molecular catalysts for CO_2 reduction to CO in flow configurations (Table S2) [54–61]. The FE_{CO} could be held at > 90% for several hours of electrolysis at 50–100 mA cm^{-2} (Fig. S13). Furthermore, we also evaluated the performance of OD-Zn based GDEs with varying CO_2 concentrations in the reactant feed at 200 mA cm^{-2} (Fig. 6c). Upon diluting the CO_2 feed, a lower FE_{CO} and higher overpotential are observed, which can be attributed to the lower concentration of CO_2 in the electrolyte. However, with only 15% CO_2 in N_2, a FE_{CO} of ~80% at 200 mA cm^{-2} can still be achieved, demonstrating the great potential of using OD-Zn for the direct conversion of flue gas from a power plant (~15% CO_2).

4. Conclusions

In summary, through electrochemical reduction of ZnO materials with very different morphologies, we synthesized three oxide-derived Zn catalysts that were highly active, selective, and stable for CO_2RR. In an H-cell reactor, all three ZnO-derived catalysts showed over 90% CO selectivity at moderate overpotentials (~750 mV) and 18 h stability. In a flow cell reactor, we achieved 91.6% CO faradaic efficiency with 200 mA cm^{-2} current density at only −0.62 V vs RHE. Ex-situ and in operando characterizations revealed that all three ZnO electrodes reconstructed to hexagonal Zn crystals during the electrochemical reduction process regardless of their preparation methods or initial morphologies. Electrochemical measurements and reaction-diffusion modelling indicated that metallic Zn is the active center for CO_2-to-CO, and the high surface area induced by reconstruction played a universal role in enhancing the geometric activity and CO selectivity of the OD-Zn catalysts. These findings highlight the importance of establishing structure-performance relationships based on the final states of the electrodes instead of the precursors, as reduction and reconstruction may dictate the overall performance. Furthermore, the electrochemical reconstruction strategy can be directly applied to other Zn compounds, including hydroxides, mixed oxides and ZnO supported materials, to synthesize advanced Zn-based catalysts for not only CO_2RR but also other important electrochemical reactions.

CRediT authorship contribution statement

Wen Luo: Conceptualization, Methodology, Data curation, Formal analysis, Writing - original draft. **Qin Zhang:** Methodology, Formal analysis. **Jie Zhang:** Methodology, Writing - review & editing. **Emanuele Moioli:** Formal analysis, Writing - review & editing. **Kun Zhao:** Formal analysis. **Andreas Züttel:** Resources, Supervision.

Declaration of Competing Interest

The authors declare that they have no known competing financial interests or personal relationships that could have appeared to influence the work reported in this paper.

Acknowledgments

This research is supported by Swiss National Science Foundation (Ambizione Project No. PZ00P2_179989). This research is also part of the activities of SCCER HeE, which is financially supported by Innosuisse-Swiss Innovation Agency.

Appendix A. Supplementary data

Supplementary material related to this article can be found, in the online version, at doi:https://doi.org/10.1016/j.apcatb.2020.119060.

References

[1] J.M. Spurgeon, B. Kumar, A comparative technoeconomic analysis of pathways for commercial electrochemical CO_2 reduction to liquid products, Energy Environ. Sci. 11 (2018) 1536–1551, https://doi.org/10.1039/c8ee00097b.
[2] S. Verma, B. Kim, H.R.M. Jhong, S. Ma, P.J.A. Kenis, A gross-margin model for defining technoeconomic benchmarks in the electroreduction of CO_2, ChemSusChem. 9 (2016) 1972–1979, https://doi.org/10.1002/cssc.201600394.
[3] M. Jouny, W. Luc, F. Jiao, High-rate electroreduction of carbon monoxide to multi-carbon products, Nat. Catal. 1 (2018) 748–755, https://doi.org/10.1038/s41929-018-0133-2.
[4] L. Wang, S.A. Nitopi, A.B. Wong, J.L. Snider, A.C. Nielander, C.G. Morales-guio, M. Orazov, D.C. Higgins, C. Hahn, F. Thomas, Electrochemically converting carbon monoxide to liquid fuels by directing selectivity with electrode surface area, Nat. Catal. 2 (2019) 702–708, https://doi.org/10.1038/s41929-019-0301-z.
[5] Y. Chen, C.W. Li, M.W. Kanan, Aqueous CO_2 reduction at very low overpotential on oxide-derived Au nanoparticles, J. Am. Chem. Soc. 134 (2012) 19969–19972, https://doi.org/10.1021/ja309317u.
[6] W. Luo, W. Xie, R. Mutschler, E. Oveisi, G.L. De Gregorio, R. Buonsanti, A. Züttel, Selective and stable electroreduction of CO_2 to CO at the copper/indium interface, ACS Catal. 8 (2018) 6571–6581, https://doi.org/10.1021/acscatal.7b04457.
[7] Y. Hori, H. Wakebe, T. Tsukamoto, O. Koga, Electrocatalytic process of CO selectivity in electrochemical reduction of CO_2 at metal electrodes in aqueous media, Electrochim. Acta 39 (1994) 1833–1839, https://doi.org/10.1016/0013-4686(94)85172-7.
[8] K. Jiang, H. Wang, W. Bin Cai, H. Wang, Li electrochemical tuning of metal oxide for highly selective CO_2 reduction, ACS Nano 11 (2017) 6451–6458, https://doi.org/10.1021/acsnano.7b03029.
[9] W. Luo, J. Zhang, M. Li, A. Züttel, Boosting CO production in electrocatalytic CO_2 reduction on highly porous Zn catalysts, ACS Catal. 9 (2019) 3783–3791, https://doi.org/10.1021/acscatal.8b05109.
[10] H.S. Lee, J. Chung, H. Shin, H. Kim, J. Koh, S.I. Woo, D.H. Won, Highly efficient, selective, and stable CO_2 electroreduction on a hexagonal Zn catalyst, Angew. Chem. Int. Ed. 55 (2016) 9297–9300, https://doi.org/10.1002/anie.201602888.
[11] J. Rosen, G.S. Hutchings, Q. Lu, R.V. Forest, A. Moore, F. Jiao, Electrodeposited Zn dendrites with enhanced CO selectivity for electrocatalytic CO_2 reduction, ACS Catal. 5 (2015) 4586–4591, https://doi.org/10.1021/acscatal.5b00922.
[12] X. Jiang, F. Cai, D. Gao, J. Dong, S. Miao, G. Wang, X. Bao, Electrocatalytic reduction of carbon dioxide over reduced nanoporous zinc oxide, Electrochem. Commun. 68 (2016) 67–70, https://doi.org/10.1016/j.elecom.2016.05.003.
[13] Y. Lu, B. Han, C. Tian, J. Wu, D. Geng, D. Wang, Efficient electrocatalytic reduction of CO_2 to CO on an electrodeposited Zn porous network, Electrochem. Commun. 97 (2018) 87–90, https://doi.org/10.1016/j.elecom.2018.11.002.
[14] D.L.T. Nguyen, M.S. Jee, D.H. Won, H.S. Oh, B.K. Min, Y.J. Hwang, Effect of halides on nanoporous Zn-based catalysts for highly efficient electroreduction of CO_2 to CO, Catal. Commun. 114 (2018) 109–113, https://doi.org/10.1016/j.catcom.2018.06.020.
[15] P. Moreno-García, N. Schlegel, A. Zanetti, A. Cedeno López, M.D.J. Gálvez-Vázquez, A. Dutta, M. Rahaman, P. Broekmann, Selective electrochemical reduction of CO_2 to CO on Zn-based foams produced by $Cu^{2+}$and template-assisted electrodeposition, ACS Appl. Mater. Interfaces. 10 (2018) 31355–31365, https://doi.org/10.1021/acsami.8b09894.
[16] T. Zhang, X. Li, Y. Qiu, P. Su, W. Xu, H. Zhong, H. Zhang, Multilayered Zn nanosheets as an electrocatalyst for efficient electrochemical reduction of CO_2, J. Catal. 357 (2018) 154–162, https://doi.org/10.1016/j.jcat.2017.11.003.
[17] K. Liu, J. Wang, M. Shi, J. Yan, Q. Jiang, Simultaneous achieving of high Faradaic efficiency and CO partial current density for CO_2 reduction via robust, noble-metal-free Zn nanosheets with favorable adsorption energy, Adv. Energy Mater. 9 (2019) 1900276, , https://doi.org/10.1002/aenm.201900276.
[18] B. Qin, Y. Li, H. Fu, H. Wang, S. Chen, Z. Liu, F. Peng, Electrochemical reduction of CO_2 into tunable syngas production by regulating the crystal facets of earth-abundant Zn catalyst, ACS Appl. Mater. Interfaces 10 (2018) 20530–20539, https://doi.org/10.1021/acsami.8b04809.
[19] D. Raciti, K.J. Livi, C. Wang, Highly dense Cu nanowires for low-overpotential CO_2 reduction, Nano Lett. 15 (2015) 6829–6835, https://doi.org/10.1021/acs.nanolett.5b03298.
[20] M. Ma, K. Djanashvili, W.A. Smith, Controllable hydrocarbon formation from the electrochemical reduction of CO_2 over Cu nanowire arrays, Angew. Chem. - Int. Ed. 55 (2016) 6680–6684, https://doi.org/10.1002/anie.201601282.
[21] M. Ma, B.J. Trzesniewski, J. Xie, W.A. Smith, Selective and efficient reduction of carbon dioxide to carbon monoxide on oxide-derived nanostructured silver electrocatalysts, Angew. Chem. - Int. Ed. 55 (2016) 9748–9752, https://doi.org/10.1002/anie.201604654.
[22] C.W. Li, M.W. Kanan, CO_2 reduction at low overpotential on Cu electrodes resulting from the reduction of thick Cu2O films, J. Am. Chem. Soc. 134 (2012) 7231–7234.
[23] H. Mistry, A.S. Varela, C.S. Bonifacio, I. Zegkinoglou, I. Sinev, Y.-W. Choi, K. Kisslinger, E.A. Stach, J.C. Yang, P. Strasser, B.R. Cuenya, Highly selective plasma-activated copper catalysts for carbon dioxide reduction to ethylene, Nat. Commun. 7 (2016) 12123, https://doi.org/10.1038/ncomms12123.
[24] S.Y. Lee, H. Jung, N.K. Kim, H.S. Oh, B.K. Min, Y.J. Hwang, Mixed copper states in anodized Cu electrocatalyst for stable and selective ethylene production from CO_2 reduction, J. Am. Chem. Soc. 140 (2018) 8681–8689, https://doi.org/10.1021/jacs.8b02173.
[25] K. Liu, J. Shen, R. Kas, W.A. Smith, In situ fabrication and reactivation of highly selective and stable Ag catalysts for electrochemical CO_2 conversion, ACS Energy Lett. 3 (2018) 1301–1306, https://doi.org/10.1021/acsenergylett.8b00472.
[26] H. Mistry, Y.W. Choi, A. Bagger, F. Scholten, C.S. Bonifacio, I. Sinev, N.J. Divins, I. Zegkinoglou, H.S. Jeon, K. Kisslinger, E.A. Stach, J.C. Yang, J. Rossmeisl, B. Roldan Cuenya, Enhanced carbon dioxide electroreduction to carbon monoxide over defect-rich plasma-activated silver catalysts, Angew. Chem. - Int. Ed. 56 (2017) 11394–11398, https://doi.org/10.1002/anie.201704613.
[27] J. Kim, W. Choi, J.W. Park, C. Kim, M. Kim, H. Song, Branched copper oxide nanoparticles induce highly selective ethylene production by electrochemical carbon dioxide reduction, J. Am. Chem. Soc. 141 (2019) 6986–6994, https://doi.org/10.1021/jacs.9b00911.
[28] H. Jung, S.Y. Lee, C.W. Lee, M.K. Cho, D.H. Won, C. Kim, H.-S.S. Oh, B.K. Min, Y.J. Hwang, Electrochemical fragmentation of Cu_2O nanoparticles enhancing selective C–C coupling from CO_2 reduction reaction, J. Am. Chem. Soc. 141 (2019) 4624–4633, https://doi.org/10.1021/jacs.8b11237.
[29] Z. Geng, X. Kong, W. Chen, H. Su, Y. Liu, F. Cai, G. Wang, J. Zeng, Oxygen vacancies in ZnO nanosheets enhance CO_2 electrochemical reduction to CO, Angew. Chem. - Int. Ed. 57 (2018) 6054–6059, https://doi.org/10.1002/anie.201711255.
[30] M. Morimoto, Y. Takatsuji, K. Hirata, T. Fukuma, T. Ohno, T. Sakakura, T. Haruyama, Visualization of catalytic edge reactivity in electrochemical CO_2 reduction on porous Zn electrode, Electrochim. Acta 290 (2018) 255–261, https://doi.org/10.1016/j.electacta.2018.09.080.
[31] D.L.T. Nguyen, M.S. Jee, D.H. Won, H. Jung, H.S. Oh, B.K. Min, Y.J. Hwang, Selective CO_2 reduction on zinc electrocatalyst: the effect of zinc oxidation state induced by pretreatment environment, ACS Sustain. Chem. Eng. 5 (2017) 11377–11386, https://doi.org/10.1021/acssuschemeng.7b02460.
[32] C. Lu, L. Qi, J. Yang, L. Tang, D. Zhang, J. Ma, Hydrothermal growth of large-scale micropatterned arrays of ultralong ZnO nanowires and nanobelts on zinc substrate, Chem. Commun. (Camb.) (2006) 3551–3553, https://doi.org/10.1039/b608151g.
[33] T. Yoshida, D. Komatsu, N. Shimokawa, H. Minoura, Mechanism of cathodic electrodeposition of zinc oxide thin films from aqueous zinc nitrate baths, Thin Solid Films 451–452 (2004) 166–169, https://doi.org/10.1016/j.tsf.2003.10.097.
[34] J.-J. Lv, M. Jouny, W. Luc, W. Zhu, J.-J. Zhu, F. Jiao, A highly porous copper electrocatalyst for carbon dioxide reduction, Adv. Mater. 30 (2018) 1803111, ,

https://doi.org/10.1002/adma.201803111.

[35] M. Li, A. Borsay, M. Dakhchoune, K. Zhao, W. Luo, A. Züttel, Thermal stability of size-selected copper nanoparticles: Effect of size, support and CO_2hydrogenation atmosphere, Appl. Surf. Sci. 510 (2020) 145439, , https://doi.org/10.1016/j.apsusc.2020.145439.

[36] W. Luo, W. Xie, M. Li, J. Zhang, A. Züttel, 3D hierarchical porous indium catalyst for highly efficient electroreduction of CO_2, J. Mater. Chem. A Mater. Energy Sustain. 7 (2019) 4505–4515, https://doi.org/10.1039/C8TA11645H.

[37] J. Zhang, W. Luo, A. Züttel, Self-supported copper-based gas diffusion electrodes for CO_2 electrochemical reduction, J. Mater. Chem. A Mater. Energy Sustain. 7 (2019) 26285–26292, https://doi.org/10.1039/C9TA06736A.

[38] J. Zhang, W. Luo, A. Züttel, Crossover of liquid products from electrochemical CO_2 reduction through gas diffusion electrode and anion exchange membrane, J. Catal. 385 (2020) 140–145, https://doi.org/10.1016/j.jcat.2020.03.013.

[39] N. Gupta, M. Gattrell, B. MacDougall, Calculation for the cathode surface concentrations in the electrochemical reduction of CO_2 in $KHCO_3$ solutions, J. Appl. Electrochem. 36 (2006) 161–172, https://doi.org/10.1007/s10800-005-9058-y.

[40] R.S. Devan, J.H. Lin, Y.J. Huang, C.C. Yang, S.Y. Wu, Y. Liou, Y.R. Ma, Two-dimensional single-crystalline Zn hexagonal nanoplates: size-controllable synthesis and X-ray diffraction study, Nanoscale. 3 (2011) 4339–4345, https://doi.org/10.1039/c1nr10694e.

[41] J. Kim, W. Choi, J.W. Park, C. Kim, M. Kim, H. Song, Branched copper oxide nanoparticles induce highly selective ethylene production by electrochemical carbon dioxide reduction, J. Am. Chem. Soc. 141 (2019) 6986–6994, https://doi.org/10.1021/jacs.9b00911.

[42] B. Kumar, V. Atla, J.P. Brian, S. Kumari, T.Q. Nguyen, M. Sunkara, J.M. Spurgeon, Reduced SnO2 porous nanowires with a high density of grain boundaries as catalysts for efficient electrochemical CO_2-into-HCOOH conversion, Angew. Chem. - Int. Ed. 56 (2017) 3645–3649, https://doi.org/10.1002/ange.201612194.

[43] F. Li, L. Chen, G.P. Knowles, D.R. MacFarlane, J. Zhang, Hierarchical mesoporous SnO_2 nanosheets on carbon cloth: a robust and flexible electrocatalyst for CO_2 reduction with high efficiency and selectivity, Angew. Chem. Int. Ed. 56 (2017) 505–509, https://doi.org/10.1002/anie.201608279.

[44] M.J. Isaacson, F.R. McLarnon, E.J. Cairns, Current density and ZnO precipitation-dissolution distributions in Zn-ZnO porous electrodes and their effect on material redistribution: a two-dimensional mathematical model, J. Electrochem. Soc. 137 (1990) 2014–2021, https://doi.org/10.1149/1.2086856.

[45] M. Michaelis, C. Fischer, L. Colombi Ciacchi, A. Luttge, Variability of zinc oxide dissolution rates, Environ. Sci. Technol. 51 (2017) 4297–4305, https://doi.org/10.1021/acs.est.6b05732.

[46] C.M. López, K.S. Choi, Electrochemical synthesis of dendritic zinc films composed of systematically varying motif crystal, Langmuir 22 (2006) 10625–10629, https://doi.org/10.1021/la0611864.

[47] S. Chen, Y. Liu, C. Shao, R. Mu, Y. Lu, J. Zhang, D. Shen, X. Fan, Structural and optical properties of uniform ZnO nanosheets, Adv. Mater. 17 (2005) 586–590, https://doi.org/10.1002/adma.200401263.

[48] R. Cuscó, E. Alarcón-Lladó, J. Ibáñez, L. Artús, J. Jiménez, B. Wang, M.J. Callahan, Temperature dependence of Raman scattering in ZnO, Phys. Rev. B - Condens. Matter Mater. Phys. 75 (2007) 1–11, https://doi.org/10.1103/PhysRevB.75.165202.

[49] D. Ren, B.S.-H. Ang, B.S. Yeo, Tuning the selectivity of carbon dioxide electroreduction toward ethanol on oxide-derived Cu_xZn catalysts, ACS Catal. (2016) 8239–8247, https://doi.org/10.1021/acscatal.6b02162.

[50] H.S. Jeon, I. Sinev, F. Scholten, N.J. Divins, I. Zegkinoglou, L. Pielsticker, B.R. Cuenya, Operando evolution of the structure and oxidation state of size-controlled Zn nanoparticles during CO_2 electroreduction, J. Am. Chem. Soc. 140 (2018) 9383–9386, https://doi.org/10.1021/jacs.8b05258.

[51] S. Nitopi, E. Bertheussen, S.B. Scott, X. Liu, A.K. Engstfeld, S. Horch, B. Seger, I.E.L. Stephens, K. Chan, C. Hahn, J.K. Nørskov, T.F. Jaramillo, I. Chorkendorff, Progress and perspectives of electrochemical CO_2 reduction on copper in aqueous electrolyte, Chem. Rev. 119 (2019) 7610–7672, https://doi.org/10.1021/acs.chemrev.8b00705.

[52] A. Wuttig, M. Yaguchi, K. Motobayashi, M. Osawa, Y. Surendranath, Inhibited proton transfer enhances Au-catalyzed CO_2 -to-fuels selectivity, Proc. Natl. Acad. Sci. U.S.A. 113 (2016) E4585–E4593, https://doi.org/10.1073/pnas.1602984113.

[53] Y.Y. Birdja, E. Pérez-Gallent, M.C. Figueiredo, A.J. Göttle, F. Calle-Vallejo, M.T.M. Koper, Advances and challenges in understanding the electrocatalytic conversion of carbon dioxide to fuels, Nat. Energy 4 (2019) 732–745, https://doi.org/10.1038/s41560-019-0450-y.

[54] T. Zheng, K. Jiang, N. Ta, Y. Hu, J. Zeng, J. Liu, H. Wang, Large-scale and highly selective CO_2 electrocatalytic reduction on nickel single-atom catalyst, Joule 3 (2019) 265–278, https://doi.org/10.1016/j.joule.2018.10.015.

[55] X. Lu, Y. Wu, X. Yuan, L. Huang, Z. Wu, J. Xuan, Y. Wang, H. Wang, High-performance electrochemical CO_2 reduction cells based on non-noble metal catalysts, ACS Energy Lett. 3 (2018) 2527–2532, https://doi.org/10.1021/acsenergylett.8b01681.

[56] S. Ren, D. Joulié, D. Salvatore, K. Torbensen, M. Wang, M. Robert, C.P. Berlinguette, Molecular electrocatalysts can mediate fast, selective CO_2 reduction in a flow cell, Science. 365 (2019) 367–369, https://doi.org/10.1126/science.aax4608.

[57] T. Haas, R. Krause, R. Weber, M. Demler, G. Schmid, Technical photosynthesis involving CO_2 electrolysis and fermentation, Nat. Catal. 1 (2018) 32–39, https://doi.org/10.1038/s41929-017-0005-1.

[58] C.-T. Dinh, F.P. Garcia de Arquer, D. Sinton, E.H. Sargent, High rate, selective and stable electroreduction of CO_2 to CO in basic and neutral media, ACS Energy Lett. 3 (2018) 2835–2840, https://doi.org/10.1021/acsenergylett.8b01734.

[59] S. Ma, Y. Lan, G.M.J. Perez, S. Moniri, P.J.A. Kenis, Silver supported on titania as an active catalyst for electrochemical carbon dioxide reduction, ChemSusChem 7 (2014) 866–874, https://doi.org/10.1002/cssc.201300934.

[60] C.M. Gabardo, A. Seifitokaldani, J.P. Edwards, C.T. Dinh, T. Burdyny, M.G. Kibria, C.P. O'Brien, E.H. Sargent, D. Sinton, Combined high alkalinity and pressurization enable efficient CO_2 electroreduction to CO, Energy Environ. Sci. 11 (2018) 2531–2539, https://doi.org/10.1039/c8ee01684d.

[61] S. Verma, Y. Hamasaki, C. Kim, W. Huang, S. Lu, H.R.M. Jhong, A.A. Gewirth, T. Fujigaya, N. Nakashima, P.J.A. Kenis, Insights into the low overpotential electroreduction of CO_2 to CO on a supported gold catalyst in an alkaline flow electrolyzer, ACS Energy Lett. 3 (2018) 193–198, https://doi.org/10.1021/acsenergylett.7b01096.